Title: Effect of microstructure on electrical and mechanical properties of $La_{5.4}WO_{12-\delta}$ proton conductor

Authors: Wendelin Deibert, Vasiliki Stournari, Mariya E. Ivanova, Sonia Escolástico, José M. Serra, Jürgen Malzbender, Tilmann Beck, Lorenz Singheiser, Olivier Guillon, Wilhelm A. Meulenberg

PII: S0955-2219(18)30208-5
DOI: https://doi.org/10.1016/j.jeurceramsoc.2018.04.009
Reference: JECS 11819

To appear in: *Journal of the European Ceramic Society*

Received date: 22-11-2017
Revised date: 4-4-2018
Accepted date: 5-4-2018

Please cite this article as: Deibert W, Stournari V, Ivanova ME, Escolástico S, Serra JM, Malzbender J, Beck T, Singheiser L, Guillon O, Meulenberg WA, Effect of microstructure on electrical and mechanical properties of $La_{5.4}WO_{12\text{-delta}}$ proton conductor, *Journal of the European Ceramic Society* (2010), https://doi.org/10.1016/j.jeurceramsoc.2018.04.009

Effect of microstructure on electrical and mechanical properties of $La_{5.4}WO_{12-\delta}$ proton conductor

Wendelin Deibert[1], Vasiliki Stournari[1,3], Mariya E. Ivanova[1], Sonia Escolástico[2], José M. Serra[2], Jürgen Malzbender[1], Tilmann Beck[4,1], Lorenz Singheiser[1], Olivier Guillon[1,5], Wilhelm A. Meulenberg[1,6]

[1]*Forschungszentrum Jülich GmbH, Institute of Energy and Climate Research IEK, D-52425 Jülich, Germany*
[2]*Universidad Politécnica de Valencia-Consejo Superior de Investigaciones Científicas, Instituto de Tecnología Química, Av. Naranjos s/n, E-46022 Valencia, Spain*

[3]*Ivoclar Vivadent AG, 9494 Schaan, Liechtenstein*

[4] *University of Kaiserslautern, Institute of Materials Science and Engineering, 67653 Kaiserslautern, Germany*
[5]*Jülich Aachen Research Alliance: JARA-Energy, Forschungszentrum Jülich GmbH, D-52425 Jülich, Germany*

[6]*University of Twente, Faculty of Science and Technology, Inorganic Membranes, P.O. Box 217, 7500 AE Enschede, The Netherlands*

*** Corresponding authors**
Dr. Wendelin Deibert
Forschungszentrum Jülich GmbH
Institute of Energy and Climate Research, IEK-1
Leo-Brandt-Str.
52425 Jülich, Germany
E-mail: w.deibert@fz-juelich.de
Tel.: 0049 (0) 24 6161 8968
Fax: 0049 (0) 24 6161 2455

Abstract

The relationships between microstructural characteristics and electrical as well as mechanical properties of $La_{5.4}WO_{12-\delta}$ (LWO54) materials were studied. Polycrystalline LWO54 samples revealed identical transport mechanisms regardless of the sample microstructure. The studied samples show predominately proton conductor behaviour below 800 ºC and become predominant n-type and oxygen ion conductors above this temperature. The magnitude of the total conductivity is enhanced with larger grain size and lower porosity. Young's modulus

decreased by 20% with increasing temperature up to 1000 °C regardless of grain size and atmosphere. Fracture strength was determined via ring-on-ring bending tests, yielding values that strongly depended on microstructural characteristics and homogeneity of the microstructure. Elevated temperature deformation studies revealed that creep is governed by cation diffusion mechanism.

Keywords: *proton-conducting ceramic membranes; lanthanum tungstate; mechanical properties; conductivity; strength; creep;*

1 Introduction

Hydrogen-related technologies receive growing attention due to the increasing importance of hydrogen as potential environmentally friendly energy carrier of the future with great social impact and economical relevance [1,2,3,4,5,6]. Therefore, proton conducting oxide ceramics [7,8,9,10,11,12,13] are at the emerging focus of materials science and process engineering. Metal-based alloys [14], including also precious metals such as Pd and Ag [15], yielding H_2-permeation in the range of few l/cm^2·min at temperatures $T \leq 500$ °C. Microporous inorganic membranes [16,17] are typically used in low temperature H_2-separation tasks. Dense ceramic membranes as studied in this work are suitable candidates, especially for applications requiring elevated temperatures (600-800 °C). First identified as mixed proton-electronic conductor by Shimura *et al.* [18], lanthanum tungstate $La_xWO_{3+1.5x}$ ($x < 6$, LWO) has been an object of intensive research during the past few years as membrane material for H_2 separation tasks or membrane reactor applications in intermediate to high temperature range [19,20,21,22,23,24,25,26,27,28,29]. In particular, LWO displays appreciable chemical and (hydro-) thermal stability [24,25], as well as relatively high values of mixed proton-electronic conductivity, after appropriate substitution, in comparison to other ceramic materials [20,23,24]. Such properties are advantageous for application, especially under highly reducing and even sulphur-containing gas environments (e.g. H_2, H_2O, CO, CO_2, CH_4, H_2S, and dust) at elevated temperatures.

In the past years, certain phase purity [21,23,30] and structural issues [31,32,33,34,35] related to this material have been identified and successfully resolved. Lanthanum tungstate was formerly referred to as La_6WO_{12}, a compound formed in the La_2O_3-WO_3 system, which was considered stable from room temperature to ~2150 °C according to [36] or existing only as a high temperature phase at T higher than ~1740 °C according to [37]. In 2001 Diot *et al.* [38] described the crystal structure as ordered defective fluorite (or disordered pyrochlores) for tungstates with small cations (such as Y and Ho) by a model applicable for RE_6WO_{12} (where RE means rare earth). However, lanthanum tungstate with 6-1-12 stoichiometry could not be synthesised as a stable compound as already reported in [21,22,23] and it finally revealed a much more complex structure for which Diot's model appeared to be unrealistic. Continuous works of Scherb [31] and Fantin *et al*. [39], independently from Magraso *et al.* [32] and Erdal *et al*. 2012 [33], have thrown light in particular on the structure of La-tungstate leading to a validated structural model of this complex compound. In addition to the electrical characteristics upon W-substitution explored in literature [23][24], structural characteristics and hydration behaviour of Re and Mo-substituted LWOs with different substitution concentration up to their solubility limits has been furthermore elucidated in a series of recent works [39] However, any further structure-related details are omitted here, reader can refer to the corresponding works. An important stoichiometry- and structure-related aspect is that the single phase region is relatively narrow (5.3-5.8 in [21]; 5.2-5.5 in [22,23]) and it reveals strong *T*-

dependent shift to higher W concentrations reflected by the increased W solubility in the La2 sites [21,32]. W^{6+} partially substituted on La^{3+} cause a decrease in oxygen vacancies concentration and leads to a structure stabilization. In this context, the total electrical conductivity of LWO increases with increasing the La/W ratio as a result of the raised oxygen vacancy concentration, but the stability of main phase suffers. Outside the aforementioned ranges of single phase stability, undesired secondary phases are typically formed e.g. free La_2O_3 at higher La/W ratios [21,22,23], and $La_6W_2O_{15}$ phase at lower La/W [22,23,30,40], both having negative impact on LWO material integrity and performance [21,22,23,30].

Apart from the complexity of composition-structure-defects-transport properties relation, partially elucidated but still requiring massive exploration effort, mechanical properties of this class of materials are scarcely considered. Various studies exist on the mechanical properties of membrane materials focusing mainly on oxygen conducting mixed ion electron conductors [41,42,43,44,45,46] but very limited contributions have been published on mechanical properties of LWO. An early study by Roa *et al.* [47] reported material hardness and Young's modulus of LWO materials with La/W ratio in the range of 4.8 - 6. The main conclusion of their work was the independence of these properties on chemical composition and sintering temperature. Furthermore the densification and variation of the particle size during sintering seems not to vary for different LWO compositions (even though containing secondary phase segregations).

As an attractive candidate for H_2 technology related applications, LWO needs to be manufactured as a membrane, often as an asymmetric structure with a porous substrate and furthermore fabricated in useful geometry and dimensions for later application. Scalable and cost effective methods for fabrication such as tape casting are more and more employed to fabricate LWO membrane components [48] and supporting components for LWO membranes [49][50]. However, for developing and optimising the procedure to fabricate defect-free components, in depth knowledge on the influence of the starting powder characteristics on the overall behaviour of ceramic body and furthermore component is required.

Similar to our earlier study on mechanical properties of tape cast porous LWO substrates [26], LWO54 will be employed as a reference composition in the present work. LWO54 stays for $La_{28-x}W_{4+x}O_{54+\delta}v_{2-\delta}$ material with $x = 1\ (\mathrm{La}/\mathrm{W} = 5.4)$ and $\delta = 1.5$, resulting in a nominal stoichiometry $La_{27}W_5O_{55.5}v_{0.5}$ (simplified from now on as $La_{5.4}WO_{11.1}v_{0.1}$ and abbreviated as LWO54). Considering different compositional and structural aspects already addressed above, it was selected as an optimal compromise between structural stability, sintering parameters and electrical behaviour amongst the range of possible LWOs with different La/W ratio. Ceramic powder with this stoichiometry is also commercially available, which makes it easily accessible for large scale fabrication routes as the tape casting. Therefore, a study has emerged which was carried out addressing LWO54 mechanical and electrical properties as a function of the characteristics of starting ceramic powder and respectively the microstructure of sintered ceramic body.

2 Experimental

2.1 Powder synthesis and sample preparation

Two different batches of LWO54 powders were used to prepare sintered samples with variable microstructure for further structural, electrical and mechanical investigations in the current work: (1) powder produced via the solid state reaction of mixed oxides and (2) commercially available powder produced by means of the spray pyrolysis with one calcination step at 600 °C in the as delivered state (Cerpotech AS, Norway).

The first LWO54 powder was synthesized following the solid state reaction (SSR) using La_2O_3 and WO_3 as starting oxides (samples labelled LWO54-SSR with a number indicating different batches). For La_2O_3 a preliminary heat treatment step was carried out at 1000 °C for two hours and the powder was weighed at a temperature of 200 °C. The oxides were then mixed in the corresponding stoichiometric ratio and heated to 1500 °C for 12 h for completion of solid state synthesis and phase formation. The resulting powder was ball-milled (24 h) and sieved afterwards.
As a second type of powder, commercially available LWO54 (Cerpotech, Norway) was used (labelled LWO54-SP). This powder was produced by spray pyrolysis and exhibited very fine particle size with a large surface area in as delivered state (labelled as LWO54-SP-1). It was additionally heat treated at 1100 °C to reduce its sintering activity for further processing (labelled LWO54-SP-2). The temperature was correspondingly selected based on the powder sintering behaviour reported elsewhere [26].
From these starting LWO54 powders samples were manufactured by isostatic pressing (pressure 400 MPa, 2 min) and sintered at 1500 °C and dwelling times up to 15 h with heating and cooling ramp of 5 K/min. All microstructural characterisations were performed with the LWO54-SSR and the LWO54-SP-2 powder because they are considered to be most relevant for future manufacturing by sequential tape casting and application.

2.2 Characterization techniques

The chemical composition of the two starting LWO54 powders was monitored by means of the Inductively-Coupled Plasma Optical Emission Spectroscopy (ICP-OES) with a device of Thermo Fisher Scientific (Germany).
The particle size distribution of the starting powders was analysed by means of laser scattering, Horiba LA-950 V2 (Horiba Europe GmbH, Germany).
Additionally, the specific surface area of the powders was determined via the BET method [51] using an AREAmeter II (Ströhlein Instruments, Germany).
Powder X-Ray diffraction (XRD) patterns were recorded in the 2θ range from 10° to 80° using D4 ENDEAVOR diffractometer by Bruker with CuKα radiation. Phase identification was carried out with ICDD PDF2-Database (Release 2004) and X'Pert Highscore Plus (PANalytical). Crystal structures were obtained from the Inorganic Crystal Structure Database (ICSD). XRD analysis was also used to monitor the samples subjected to conductivity measurements for possible structural changes in a post-mortem state. For this purpose, XRD patterns were recorded in the 2θ range from 20 to 90º on a PANalytical CubiX FAST equipment using CuK_α radiation.
Microstructural analysis of sintered LWO54 samples were performed either via the SEM using a "Phenom" (FEI) with a backscattered electron detector and acceleration voltage of 5 kV. To analyse the porosity of the sintered LWO54 specimens, multiple SEM images of sample cross-sections were recorded and analysed by means of AnalysisPro image analysis software (Olympus).
The sintering behaviour of the different LWO54 pressed powder samples was investigated by means of an optical dilatometer "TOMMI plus" from Fraunhofer ISC Würzburg, Germany. The basic principle of the instrument is to record images of the samples' silhouette by a CCD-camera during the heat treatment. To achieve a high contrast, a monochromatic light source is mounted opposite to the camera. For the measurements, a heating ramp of 5 K/min and temperature of 1500 °C with dwelling times of up to 15 h were used. Pictures of the samples silhouettes were taken every 60 s during the heat treatments and data were analysed by means of specialized software "TOMMI online".
Electrical conductivity measurements were performed by four-point DC technique supplying a constant current by a programmable current source (Keithley 2601), while the voltage drop through

the sample was detected by a multimeter (Keithley 3706). Bars were contacted with silver paste and wire. Conductivity tests were performed in different atmospheres studying the hydration and H/D isotopic effect in reducing conditions using 5 % H_2 in He (dry conditions), 5 % H_2 in He saturated in H_2O (2.5 %), 5 % D_2 in He (dry conditions) and 5 % D_2 in He saturated in D_2O (2.5 %).
In order to investigate the effect of temperature and atmosphere on dense LWO54 material, extended analysis of Young's modulus was performed with various tests, namely indentation, impulse excitation and ring-on-ring bending tests, see also [52,53,54,55,56].
The indentation tests were carried out using a Fischer HC100 (Helmut Fischer KG, Sindelfingen) indentation system. A load of 1 N was applied to test the materials properties. The analysis was carried out based on the DIN ISO 14577-1. An impulse excitation instrument (GrindoSonic J.W. Lemmens N.V, Belgium) was used for elastic modulus determination using bar-shaped specimens. Measurements were carried out in air and Ar/4% H_2 atmospheres, in a temperature range from room temperature to 1000 °C with heating rate of 5 K/min. The calculations of elastic modulus were based on ASTM standard E 1876-01 [57].
Elastic modulus and fracture stresses from RT up to 1000 °C were determined using bi-axial ring-on-ring bending test following ASTM C1499 [58]. Fractography was also applied to the broken tested pieces to characterize the failure origins. Fracture surfaces were analysed by SEM Zeiss SUPRA 50VP. Details of the ring-on-ring fracture tests along with the equations used for evaluation have been reported elsewhere [59]. The experiments were carried out with an electromechanical testing machine (Instron 1362). The central displacement was measured with a sensor attached to the tensile-loaded sample surface. A ceramic extension rod connected to a linear variable differential transformer (Sangamo, range ±1 mm, precision 1.25 µm) provided the value of actual displacement. The load measurements were performed with a 1.5 kN load cell (Interface 1210 BLR). The loading rates were between 1 and 1000 N/min for room temperature measurements in air. For tests at temperatures between 400 and 1000 °C the loading rate was kept constant at 100 N/min. Samples dimensions were according to DIN 51105:2010-08 [60]. Tests were performed from room temperature up to 1000 °C with a heating rate of 8 K/min. Characteristic strength σ_0 and Weibull modulus m were derived using a maximum likelihood method according to ASTM C1239-07 [61]. Fractography was applied according to ASTM 1322 [62].
Compressive creep tests were performed at applied stresses σ between 20 and 63 MPa. The tests were carried out in air (p_{O2} of 200 mbar) at selected temperatures in the range from 700 °C to 1450 °C with temperature increments of 100 K or 150 K. Characteristics of the samples tested for creep in compression are listed in Table 1. The experimental setup as well as the evaluation procedure are described elsewhere [63].Each creep measurement was terminated after at least 24 h of a steady-state deformation or until an integral deformation of 100 µm was reached.

3 Results and Discussion

3.1 Powder characterisation

The two methods of powder preparation led to different powder properties with respect to particle size, specific surface area, and particle morphology, on which the sintering behaviour and finally the microstructure in sintered state are strongly dependent.
The particle size distributions of the in-house synthesised LWO54-SSR-1 powder and the commercial LWO54-SP-2 powder (calcined at 1100 ºC) are shown in Figure 1, while powder properties are listed in Table 2. Although the D_{50} value is almost the same for both powders, the particle size distribution

and the specific surface area are different. Higher surface area usually leads to a stronger densification during sintering.

3.2 Sintering studies

3.2.1 Shrinkage measurements

Shrinkage measurements were performed with an optical dilatometer as outlined in the experimental part. The results obtained for the two powders LWO54-SSR and LWO54-SP are shown in Figure 2. The samples were heated up to 1500 °C and held at this temperature for 10 h. The shrinkage of the LWO54-SP powder was 20 % and thus higher and it started earlier than the LWO54-SSR (shrinkage ca. 10 %) due to the higher sintering activity. This is a consequence of the synthesis method, which led to a higher specific area of the powder (Table 2). After about two hours of holding time the maximum density (of about 98%) of both powders was reached.

3.2.2 Microstructure

The porosity development during the sintering of LWO54-SSR and LWO54-SP-2 is shown in Figure 3. For this purpose, SEM and image analysis software were employed to analyse cross-sections of multiple pellets sintered at different temperatures or holding times. Samples prepared from LWO54-SP powder showed a faster densification behaviour attributed to the higher sintering activity related to the synthesis process. A gradual porosity decrease of around 10% is observed for both samples in the temperature range 1200 °C -1400 °C. The major densification stage takes place at temperatures above 1400 °C. Above this temperature, a significant drop in porosity from 30 to 13% and from 25 to 3% is observed for the SSR and SP samples, respectively. In the isothermal domain, the first 3 hours play an important role, especially in the case of the SSR samples. Longer dwell times are not beneficial for further decrease of porosity. Figure 4 shows selected SEM-images of the microstructure of polished sintered SSR- and SP-derived samples.

The evolution of the grain sizes is illustrated in Figure 5, as derived from SEM analysis by the line intercept method. Starting at 1500 °C with no holding time, the grain size of samples derived from both powders increases with the dwell time up to 13-15 µm. After 15 h the LWO54-SP-2 sample revealed a slightly higher average grain size than the LWO54-SSR sample. A massive grain growth is visible during the given dwell time so that porosity is entrapped within the grains.

3.3 Electrical conductivity

Total conductivity under reducing conditions for the samples LWO54-SSR-1, LWO54-SSR-2 and LWO54-SP-2 was studied, aiming to discern the effect of the microstructure on the transport processes. Table 3 summarizes the sintering temperature and the microstructural data of the employed samples.

Figure 6 shows the total conductivity as a function of the inverse temperature in dry and wet H_2 and D_2 atmospheres (where H_2 and D_2 are diluted in 95 % helium and wet means pH_2O and pD_2O values of 0.025 atm).

The predominant transport mechanisms depending on the temperature appear to be the same, irrespectively of the microstructure properties. Indeed, the three compounds present a prevailing proton transport up to 800 ºC, as inferred from the isotopic effect ($\sigma_{H_2+H_2O} > \sigma_{D_2+D_2O}$) and the hydration effect ($\sigma_{H_2+H_2O} > \sigma_{H_2}$ and $\sigma_{D_2+D_2O} > \sigma_{D_2}$), in agreement with previous reports

[20,34,27]. Both *n*-type and oxygen-ion conduction become predominant with respect to the proton conduction at higher temperatures as can be deduced from the negligible isotopic and hydration effect above 800 ºC and this is in line with the progressive oxide dehydration at high temperatures.

A comparison of the conductivity under wet H_2 and D_2 is presented in Figure 7.The highest conductivity is observed for LWO54-SSR-2 and this is ascribed to both, larger grain size and lower porosity than LWO54-SSR-1. On the other hand, LWO54-SP-2 presents slightly higher conductivities than LWO54-SSR-1, especially at low temperature, which can also be related to the lower porosity and larger grain size of LWO54-SP-2. These results evidence the relevance of microstructural aspects on conduction behaviour in this kind of materials.

XRD was used to characterize the phase composition and structural characteristics of the LWO54 samples after conductivity measurements and the results are shown in Figure 8 (logarithmic scale in y-axis). For all samples a cubic fluorite structure could be confirmed. Minor diffraction peaks related to different impurities such as La_2O_3 and $La_6W_2O_{15}$ were also be detected but an important influence on the conductivity values cannot be expected. Diffraction peaks corresponding to the sample holder and silver from the contacts are labelled as * and +, respectively.

3.4 Mechanical properties

3.4.1 Elastic modulus

The samples were tested regarding Young's Modulus via the three different methods, indentation testing, impulse excitation technique (IET) and ring-on-ring bending (R-o-R). All samples were tested via indentation test and R-o-R, while LWO54-SSR-1 and LWO54-SP-2 specimens were also tested by impulse excitation technique in air to derive representative data for the temperature dependency of the elastic modulus. In addition, LWO54-SSR-2 was also tested in Ar/4% H_2. The derived data are compiled in Table 4. The elastic modulus was independent on the grain size with a value of ~ 140 GPa at room temperature, as can be seen in Figure 9. Overall, the values at room temperature are in good agreement with the results obtained via the indentation technique (see Table 4, Figure 9 and Figure 10) and also those quoted in literature [47], although for LWO54-SP-2 the impulse excitation technique yielded a slightly higher value than the indentation test method, probably due to the lower porosity of that sample (Table 3).

Generally, the elastic modulus of polycrystalline ceramics, without grain boundary softening, is expected to decrease by ~ 1 % per hundred Kelvin [64]. For LWO54 a decrease by ~ 20 % up to 1000 °C is observed for both samples independent on the atmosphere and the grain size. A change in the slope is indicated at ~ 400 °C and subsequently the elastic modulus decrease is less pronounced with increasing the temperature up to 1000 °C.
The temperature dependence of Young's modulus of ceramic materials can also be generally described according to Hillig [65]:

$$\frac{E}{E_0} = 1 - \left(\frac{T}{T_m}\right)^3 \quad (1)$$

where E_0 is the Young's modulus at room temperature, and T_m is the melting temperature of the material. E_0 = 140 GPa with a melting temperature of T_m = 1960 °C (from the phase diagram La_2O_3-WO_3 [37]) was used. The model predicts that the elastic modulus decreases by ~ 20 % up to 1000 °C, similar to the experimental results. The kink at ~ 400 °C might be attributed to chemical or thermal

expansion related effects at this temperature. Indeed, reported TGA measurements after permeation tests revealed a weight loss at 400 °C temperature suggesting oxygen release from the matrix [24].

The LWO54 materials were also tested using ring-on-ring testing in order to assess potential microstructural effects at room temperature. Here, the tested batches were LWO54-SSR-1, LWO54-SP-1 and LWO54-SP-2. Elevated temperature tests were only carried out for samples composed of the commercial powder LWO54-SP-1, see Figure 10. Batch LWO54-SP-2 was also tested at elevated temperatures but samples broke during heating before the measurement started. The reason will be discussed later in the fractography analysis.

The results indicate an average elastic modulus of ~ 120 GPa at room temperature for all tested materials (Table 4), similar as obtained by the other methods, slight differences in local properties, that appeared to be reflected in the indentation results, are not visible in the global bending test data. The effect of temperature on the elastic modulus was investigated for the LWO54-SP-1 batch. The elastic modulus decrease with increasing temperature agrees with the impulse excitation result, although at ~ 350 °C a slight increase is observed, whereas in the impulse excitation a kink was observed at ~ 400 °C suggesting that the onset of chemical or thermal expansion differences might affect both testing results in a different way. However, the difference in the temperature between the two methods, i.e. where the kink is observed, is not varying much considered that the oven /thermocouples in the bending test setup is not very accurate in this low temperature range.

3.4.2 Fracture strength

Ring-on-Ring fracture stress measurements were performed at room temperature for batches LWO54-SSR-1, LWO54-SP-1 and LWO54-SP-2, see Table 5. Overall, mean fracture stresses are in good agreement with characteristic strengths estimated via Weibull analysis.

Additionally, a set of experiments was performed at room temperature with different loading rates to assess possible subcritical crack growth effects. Furthermore, the LWO54-SP-1 batch was also tested at 1000 °C in order to determine the elevated temperature fracture stress. Note that according to industrial standards the specimen number was too low for a Weibull analysis; hence it should only serve as an indication of the materials behaviour.

The LWO54 material prepared by solid state synthesis route (LWO54-SSR) revealed a two times higher strength and average fracture stress than the batches prepared from commercial powder (LWO54-SP-1 and LWO54-SP-2). This fact can be related to its more homogeneous microstructure (see Figure 12, showing the microstructure of the three specimens). The differences in fracture stress are also reflected in fracture strain, where the values are higher for the LWO54-SSR batch. When comparing the LWO54-SP batches, LWO54-SP-2 exhibited lower strength, and their microstructure was rather homogeneous with similar porosity. Therefore, the values appear also to reflect the effect of the grain size on strength. Larger grain sizes are known to lead to lower strengths [66].
Fractography analysis revealed the failures origins in LWO54-SP batches. In the case of LWO54-SP-2, large agglomerates and irregular pores in the bulk were found as typical failure origins. Pore zones located either under the surface and in the bulk were identified as failure origins in case of LaWO54-SP-2 (Figure 11). Regarding LWO54-SSR batch, it exhibits high energy fracture patterns, thus the

possible failure origin defects were small and could not be located. It seems that by controlling the manufacturing process, thus the microstructure, strength can be increased by a factor of ~2.
The average fracture stress based on five specimens each was measured for loading rates of 1, 100 and 1000 N/min for LWO54-SP-1 in order to investigate if the material is prone to subcritical crack growth (SCG) [67].Resulting values were around 60 MPa for all loading rates and agreed within the limits of uncertainty, indicating that there was no pronounced effect of subcritical crack growth. The reason for this could also be related to (i) small number of testing specimens, (ii) measurement uncertainties by using the ring-on-ring method. Nevertheless elevated temperature subcritical crack growth studies should be the aim of suture investigations since effects under this conditions, especially in humid atmosphere, might be more pronounced.
Another set of experiments was performed also for the LWO54-SP-1 batch to characterize its elevated temperature average fracture stress. The results are illustrated in Figure 13. Due to the limited number of tested specimens Weibull statistics was not applied and only mean values are presented. Testing of LWO54-SP-2 samples was not possible since specimens broke during heating as mentioned above. The reason for this could be that a densified rim was developed during pressing at the edge of the specimens. The areas with different press density were densifying differently resulting in stress development.

The strength of most ceramics decreases monotonously with increasing temperatures. In the case of LWO54, an unusual increase in average fracture stress is observed at 400 °C from 56 ± 7 to 100 ± 8 MPa (note, at this temperature also the elastic modulus increased). At higher temperatures (600 – 1000 °C), the average fracture stress decreases again. The overall decrease from room temperature to 1000 °C was ~ 45 %.
A set of experiments was performed at 400 °C with different heat treatment in order to determine if this unusual behaviour is related to chemical strain effects. One specimen was heated up to 1000 °C and then cooled down to 400 °C and tested and another sample was heated up to 400 °C, and the load was applied after 12 hours dwell time. XRD analysis did not indicate any effects related to phase changes.
Whereas the sample tested after cooling down revealed almost the same fracture stress (see Table 6), the dwelled sample showed a 20 % lower fracture stress. In case of chemical expansion, dwelling at a particular temperature can lead to the relaxation of induced stresses. However, no significant effect on elastic modulus was observed, which was increased to a lower extent anyway. Although being an initial indication, more scientific works focusing on this aspect would be required to verify and explain the effect in more detail, which was out of the scope of the current study.

3.4.3 Creep

Samples of batches LWO54-SSR-1, LWO54-SSR-2 and LWO54-SP-2 were tested with respect to creep deformation. The selection criterion was based on the grain sizes of the samples; therefore LWO54-SP-1, which has the same grain size as LWO54-SSR-2 was excluded from the test series.
The Arrhenius plots for all compositions in air for applied stresses of 40 and 63 MPa are presented in Figure 14.
LWO54-SSR-2 material (mean grain size of ~ 11 µm) was tested over the temperature range 700 – 1450 °C ($0.43 \leq T/T_m \leq 0.77$) in air at nominal stresses of 20 – 63 MPa. Indications of creep deformation were observed above 900 °C for 63 MPa. However, at this temperature the deformation rate was close to the limit of measurement uncertainty (~1 µm / 24 hours), therefore, only the creep rates at $T \geq 1150$ °C were used for the creep analysis. Creep deformation seems to be insignificant at the operation relevant temperatures of 600 – 800 °C for dense LWO54 materials. The stability criterion suggested in literature requires the creep strain rate to stay below 1 % per year

[68]. Therefore, regarding to its creep behaviour, LWO seems to be a suitable candidate material for membrane application. The effect of porosity on creep is also of great importance for this material since it will lead to higher creep rates [69,70] and it should be taken into consideration.
Furthermore, creep rates obtained at 1050 °C for LWO54-SSR-2 during a heating and cooling thermal cycle (Figure 14b, red circle, closed and red open respectively) are almost identical thus excluding a hysteresis effect (see [71,72]). The difference between the values is ~ 14 % and it is in the limits of the measurement error at this temperature, where deformation is still low for this material. The obtained creep rates were similar for LWO54-SSR-2 and LWO54-SP-2 materials, while LWO54-SSR-1 revealed higher creep rates as can be seen in Figure 14.
The creep parameters were determined by multi-linear fitting of the general creep equation that has been widely used for creep characterization of ceramic membrane materials [73]:

$$\dot{\varepsilon} = A \cdot \left(\frac{1}{d}\right)^{p} \cdot \sigma^{n} \cdot exp\left(-\frac{Q_a}{RT}\right) \quad (2)$$

Where d is the grain size, n the stress exponent, Q_a the activation energy, R the universal gas constant and A a proportionality constant.
The activation energies, stress exponents and inverse grain size exponent (p) are presented in Table 7, Table 8 and Table 9, respectively.

Overall, from all data, an average activation energy of 450 ± 35 kJ/mol for 1250 – 1350 °C at 40 MPa along with an average stress exponent of 1.2 ± 0.4 for 1050 – 1450 °C for all materials indicate a diffusional aided creep mechanism.
Furthermore, the stress exponents are close to unity and increase slightly with temperature for the LWO54-SSR-2 material. The jump to n ~ 1.7 at 1350 °C was biased by primary creep effects for the respective material. The inverse grain size exponent p in Table 9 is independent on stress but decreases with increasing the temperature.

In general, the various possible creep mechanisms give rise to different combinations of n and p exponents so that the transitions from one mechanism to another could be defined. At 1150 °C, only LWO54-SSR-2 material was tested (grain size ~ 11 µm). At this temperature, p presents a value of ~ 2 (note that p only changes for temperature not for each compound), and n is approximately 1. This combination suggests a diffusional creep mechanism, where the diffusion path could be either along the grain boundaries (Coble model) [74] or through the grains (Nabarro, Herring) [75,76]. With increasing temperature at 1250 °C, p slightly decreases to ~ 1.5. For LWO54-SSR-1 and LWO54-SSR-2 materials (grain size up to ~ 10 µm), the stress exponent is close to 1, while for LWO54-SP-2 with slightly larger grains (~ 17 µm) the stress exponent is higher (n ~ 1.7). The combination of $1 < p < 2$ and n ~ 1 found for the LWO54-SSR-1 and LWO54-SSR-2 materials suggests a diffusional mechanism. In the case of LWO54-SP-2, additional mechanisms could contribute to the creep.
An increase to a temperature of 1350 °C leads to a decrease of p from 1.5 at 1250 °C to 0.8 (hence p is taken to be close to 1). For LWO54-SSR-2 the stress exponent n is close to 1. Since there is no theoretical creep mechanism prediction for the combination of n ~ 1 and p ~ 1, it is assumed that other mechanisms contribute to the creep deformation and there might be a transition to grain boundary sliding.
In Table 7, the evolution of the activation energy versus temperature for all materials is presented. The activation energy for LWO54-SSR-2 material at this temperature agrees with the diffusion coefficient for La diffusion through grain boundaries reported by Vøllestad *et al.* [77]. They communicated activation energies of 410 ± 30 kJ/mol and 450 ± 30 kJ/mol for La and W, respectively, for 1150 – 1350 °C in air and 5 % H_2 / Ar. The diffusion coefficient for La diffusion through grain boundaries was determined to be 170 ± 50 kJ/mol. It was concluded that this reflects

the migration via a common migration mechanism for both species, facilitated by vacancies on the lanthanum sub-lattice.

From Table 7, it can be seen that the activation energy is grain size and temperature dependant. In case of LWO54-SP-2 material, with larger grains, a very low deformation was measured in the low temperature (below 1250 °C). For the materials with smaller and larger grain size, LWO54-SSR-1 & LWO54-SP-2, respectively, in the temperature range of 1250 – 1350°C, an increase of the activation energy from 420 kJ/mol to 565 kJ/mol was detected.

The movement of single atoms or ions drives the diffusional creep either by grain boundary diffusion (Coble creep [74]) or by lattice diffusion (Nabarro-Herring creep [75,76]). Hence, the Nabarro-Herring creep is controlled by the lattice diffusivity and Coble creep by the grain boundary diffusivity. Regarding the LWO54-SSR-1 and LWO54-SSR-2 materials with the smaller and intermediate grain size respectively, they both yielded measurable deformation in the whole temperature range of 1050 °C – 1350 °C and a transition to higher activation energy was observed at T > 1250 °C resulting in a kink in the Arrhenius plot (Figure 14b & and Table 7). The effect is more profound for LWO54-SSR-2 with the intermediate grain size. This effect is also in good agreement with the theory for diffusional creep and it can be again attributed to a transition from Nabarro (lattice) to Coble (grain boundaries) mechanism, since the higher sensitivity to grain size allows Coble creep to dominate over Nabarro-Herring at lower temperatures and smaller grain size. To verify the hypothesis as well as to clarify the mechanism studies with a broader grain size range would be required in future works. Note, the activation energies reported by Vøllestad *et al.* [77] are similar to the ones obtained for $T \geq 1250$ °C. Overall, migration seems to occur via a common migration mechanism for both species (La or W) via both, lattice and grain boundaries.

4 Conclusions

This works addresses the study of LWO54 mechanical and electrical properties as a function of the characteristics of starting ceramic powder and respectively the microstructure of sintered ceramic body.

The microstructure influence on conduction behaviour and mechanical properties of LWO54 was studied at high temperatures. The studied compounds presented the same predominant transport mechanisms irrespectively of the microstructural characteristics, i.e. they are mainly protonic conductors below 800 ºC and become predominant *n*-type and oxygen ion conductors above this temperature. However, the magnitude of the total conductivity depends on the microstructure properties, increasing with the increasing grain size and decreasing porosity.

The room temperature Young's modulus is between 120 and 140 GPa, independent on the grain size, while a decrease in Young's modulus by ~ 20 % was observed up to 1000 °C independent of the atmosphere.

Ring-on-ring bending test on dense LWO54 characteristic strength of σ_0 = 59 ± 3 MPa. It was shown that a factor ~ 2 higher strength value could be obtained for homogeneous microstructure (σ_0 =124 ± 6 MPa for dense LWO54 from SSR powder).

Large agglomerates, irregular pores and pore zone areas were identified as strength limiting flaws by fractography analysis for the LaWO54-SP materials. Strength was found to decrease by ~ 30 % up to 1000 °C. An unexpected strength increase by ~ 45 % at 400 °C in comparison to strength measured at RT was observed. Complementary annealing studies indicated a relationship to the onset of chemical / thermal expansion, where longer annealing leads to lower strength values.

Extensive elevated temperature deformation studies revealed that LWO54 creep is governed by cation diffusion as the predominant mechanism. The migration appears to be a combination of

cations along grain boundaries and / or lattice. Overall, it seems that LWO54 regarding to its creep behaviour, seems to be a suitable candidate material for membrane application.

Acknowledgments

This work was conducted thanks to the financial support by the Helmholtz Association, Initiative and Networking Fund, MEM–BRAIN Portfolio and POFIII. The colleagues from ZEA-3 are acknowledged for performing the ICP-OES analysis. We would like to thank Ms. Tatjana Osipova for the mechanical testing and Dr. Egbert Wessel for the SEM studies.

References

1 C. Higman, M. van der Burgt, Gasification (2nd Edition), ISBN 9780750685283 (Print Book); ISBN 9780080560908 (eBook), Elsevier (2008).

2 B. Sorensen, Hydrogen and Fuel Cells (2nd Edition), ISBN 9780123877093 (Print Book); ISBN 9780123965035 (eBook), Elsevier (2011).

3 J. Franz, Dissertation, ISBN 978-3-8440-1677-2, Verlag Shaker, Reihe: Berichte aus der Energietechnik, Ruhr-Universität Bochum (2012).

4 S. T. Schiebahn, Dissertation, Effizienzoptimierte CO_2-Abtrennung in IGCC-Kraftwerken mittels Wassergas-Shift-Membranreaktoren, ISSN 1866-1793, ISBN 978-3-89336-958-4, Schriften des Forschungszentrums Jülich, Reihe Energie & Umwelt / Energy & Environment, Band/Volume 213, RWTH Aachen University, (2013).

5 I. Dincer, C. Zamfirescu, Advanced Power Generation Systems (1st Edition), ISBN 9780123838605 (Print Book); ISBN 9780123838612 (eBook), Elsevier (2014).

6 M. Stoukides, Solid-Electrolyte Membrane Reactors: Current Experience and Future Outlook, Catalysis Reviews: Science and Engineering, 42(1-2), 1-70 (2000).

7 H. Iwahara, T. Esaka, H. Uchida, N. Maeda, Proton conduction in sintered oxides and its application to steam electrolysis for Hydrogen production, Solid State Ionics 3/4, 359-363 (1981).

8 T. Norby, Proton conduction in oxides, Solid State Ionics 40/41, 857-862, (1990).

9 T. Norby, Proton conductivity in perovskite oxides, Chapter 11 in Perovskite Oxides for Solid Oxide Fuel Cells, Fuel Cells and Hydrogen Energy, 217-241, T. Ishihara (Ed.), doi: 10.1007/978-0-387-77708-5_11, Springer Science+Business Media, LLC (2009).

10 K.D. Kreuer, Proton Conductivity: Materials and Applications, Chem. Mater. *8*, 610-641 (1996).

11 K.D. Kreuer, Proton-conducting oxides, Annu. Rev. Mater. Res., 33:333–59, (2003).

12 N. Bonanos, Oxide-based protonic conductors: point defects and transport properties, Solid State Ionics 145, 265–274, (2001).

13 T. Schober, Applications of oxidic high-temperature proton conductors, Solid State Ionics 162– 163, 277– 281 (2003).

14 G. Alfeld, J. Viilkl, Hydrogen in Metals I- Basic properties, G. Alfeld, J. Volkl (Edts.), Berlin and New York, Springer-Verlag, Topics in Applied Physics, Vol. 28, p. 442 (1978).

15 A. Basile, F. Gallucci, S. Tosti, Chapter 8 in Membrane Science and Technology, Volume 13, Elsevier B.V., ISSN 0927-5193, DOI: 10.1016/S0927-5193(07)13008-4 (2008).

16 T. van Gestel, D. Sebold, F. Hauler, W.A. Meulenberg, H.-P. Buchkremer, J. Membr. Sci. 359, 64, (2010).

17 C. Feng, K.C. Khulbe, T. Matsuura, R. Farnood, A.F. Ismail, Recent Progress in Zeolite/Zeotype Membranes, J. Mem. Sci. Res. 1, 49-72 (2015).

18 T. Shimura, S. Fujimoto, H. Iwahara, Solid State Ionics 143, 117−123 (2001).

19 R. Haugsrud, Defects and transport properties in Ln_6WO_{12} (Ln = La, Nd, Gd, Er). Solid State Ionics, 178 (7-10), p. 555-560 (2007).

20 R. Haugsrud, C. Kjølseth, Effects of protons and acceptor substitution on the electrical conductivity of La_6WO_{12}, Journal of Physics and Chemistry of Solids 69, 1758–1765 (2008).

21 A. Magrasó, C. Frontera, D. Marrero-Lopez, P. Núñez, New crystal structure and characterization of lanthanum tungstate "La_6WO_{12}" prepared by freeze-drying synthesis, Dalton Transactions, 46, p. 10273-10283, (2009).

22 J. Seeger, Dissertation, Entwicklung protonenleitender Werkstoffe und Membranen auf Basis von Lanthan-Wolframat für die Wasserstoffabtrennung aus Gasgemischen, ISSN 1866-1793, ISBN 978-3-89336-903-4, Schriften des Forschungszentrums Jülich Reihe Energie & Umwelt/Energy & Environment, Band/Volume 188, Ruhr-Universität Bochum (2013).

23 J. Seeger, M. E. Ivanova, W. A. Meulenberg, D. Sebold, D. Stöver, T. Scherb, G. Schumacher, S. Escolástico, C. Solís, J. M. Serra, "Synthesis and characterization of non-substituted and substituted proton-conducting $La_{6-x}WO_{12-\delta}$", Inorganic Chemistry 52, 10375 (2013).

24 S. Escolástico, J. Seeger, S. Roitsch, M. E. Ivanova, W.A. Meulenberg, J.M. Serra, ChemSusChem, 6, 1523 (2013).

25 D. van Holt, E. Forster, M. E. Ivanova, W.A. Meulenberg, M. Müller, S. Baumann, R. Vaßen, "Ceramic materials for H2 transport membranes applicable for gas separation under coal-gasification-related conditions" J. Eur. Cer. Soc. 34, 2381–2389 (2014).

26 W. Deibert, M. E. Ivanova, W. A. Meulenberg, R. Vaßen, O. Guillon, "Preparation and sintering behaviour of $La_{5.4}WO_{12-\delta}$ asymmetric membranes with optimised microstructure for hydrogen separation", J. Mem. Sci., 492, 439-451 (2015).

27 S. Escolástico, C. Solís, T. Scherb, G. Schumacher, and J. M. Serra, "Hydrogen separation in La5.5WO11.25−δ membranes," *Journal of Membrane Science*, vol. 444, pp. 276-284, 2013.

28 S. Escolástico, C. Solís, J.M. Serra. Study of hydrogen permeation in (La 5/6Nd 1/6) 5.5WO 12-δ membranes, Solid State Ionics, 216, 31-35, 2012.

29 C. Solís, S. Escolástico, R. Haugsrud, J.M. Serra. $La_{5.5}WO_{12-\delta}$ characterization of transport properties under oxidizing conditions: A conductivity relaxation study, Journal of Physical Chemistry C, 115, 11124-11131, 2011.

30 M.E. Ivanova,et al., Influence of the $La_6W_2O_{15}$ phase on the properties and integrity of $La_{6-x}WO_{12-\delta}$ based membranes. Chemistry and Materials Research, 2(1), 56-81 (2012).

31 T. Scherb, Dissertation, Strukturelle Charakterisierung von Wasserstoff trennenden Gasseparationsmembranen auf Lanthanoid-Wolframat-Basis, Technische Universität: Berlin. (2011).

32 A. Magrasó, J. M. Polfus, C. Frontera, J. Canales-Vazquez, L.-E. Kalland, C. H. Hervoches, S. Erdal, R. Hancke, M. Saiful Islam, T. Norby, R. Haugsrud, Complete structural model for lanthanum

tungstate: a chemically stable high temperature proton conductor by means of intrinsic defects, Journal of Materials Chemistry, 22(5), 1762-1764 (2012).

33 S. Erdal, L.E. Kalland, R. Hancke, J. Polfus, R. Haugsrud, T. Norby, A. Magrasó, Defect structure and its nomenclature for mixed conducting lanthanum tungstates $La_{28-x}W_{4+x}O_{54+3x/2}$, Int. J. Hydr. Energ. 37, 8051-8055 (2012).

34 A. Magrasó, R. Haugsrud, Effects of the La/W ratio and doping on the structure, defect structure, stability and functional properties of proton-conducting lanthanum tungstate $La_{28-x}W_{4+x}O_{54+\delta}$. A review, Journal of Materials Chemistry A, 2 (32), 12630-12641 (2014).

35 T. Scherb, S. A. J. Kimber, C. Stephan, P. F. Henry, G. Schumacher, S. Escolastico, *et al.*, "Nanoscale order in the frustrated mixed conductor La5.6WO12-delta," *Journal of Applied Crystallography*, vol. 49, pp. 997-1008, Jun 2016.

36 M. M. Ivanova, G.M. Balagina, E.Ya. Rode, Izv. Akad. Nauk SSSR, Neorg. Mater. 6, 914 (1970).

37 M. Yoshimura, A. Rouanet: High Temperature Phase Relation in the System La_2O_3-WO_3, Mater Res. Bull. 11(2), 151-158 (1976).

38 N. Diot, O. Larcher, R. Marchand, J.Y. Kempf, P. Macaudière: Rare-earth and tungsten oxynitrides with a defect fluorite-type structure as new pigments; J. Alloys Compd. 323-324, 45-48 (2001).

39 A. Fantin, T. Scherb, J. Seeger, G. Schumacher, U. Gerhards, M. E. Ivanova, *et al.*, "Crystal structure of Re-substituted lanthanum tungstate La5.4W1−yReyO12–δ(0 ≤y≤ 0.2) studied by neutron diffraction," *Journal of Applied Crystallography*, vol. 49, pp. 1544-1560, 2016.

40 M.H. Chambrier, R. M. Ibberson, F. Goutenoire, Structure determination of α–$La_6W_2O_{15}$, J. Solid State Chem. 183, 1297–1302 (2010).

41 G. Pećanac, S. Baumann, J. Malzbender, Mechanical properties and lifetime predictions for $Ba_{0.5}Sr_{0.5}Co_{0.8}Fe_{0.2}O_{3-\delta}$ membrane material, J. Membr. Sci., 385–386 (2011), pp. 263–268

42 B.X. Huang, J. Malzbender, R.W. Steinbrech, P. Grychtol, C.M. Schneider, L. Singheiser, Anomalies in the thermomechanical behavior of $Ba_{0.5}Sr_{0.5}Co_{0.8}Fe_{0.2}O_{3-\delta}$ ceramic oxygen conductive membranes at intermediate temperatures, Appl. Phys. Lett., 95 (2009), 051901

43 B. Huang, J. Malzbender, R.W. Steinbrech, Elastic anomaly and internal friction of $Ba_{0.5}Sr_{0.5}Co_{0.8}Fe_{0.2}O_{3-\delta}$ and $La_{0.58}Sr_{0.4}Co_{0.2}Fe_{0.8}O_{3-\delta}$, J. Mater.Res., 26 (2011), pp. 1388–1391

44 W. Araki, Y. Arai, J. Malzbender, Transitions of $Ba_{0.5}Sr_{0.5}Co_{0.8}Fe_{0.2}O_{3-\delta}$ and $La_{0.58}Sr_{0.4}Co_{0.2}Fe_{0.8}O_{3-\delta}$, Mater. Lett., 132 (2014), pp. 295–297

45 B.X. Huang, J. Malzbender, R.W. Steinbrech, L. Singheiser, Mechanical properties of $La_{0.58}Sr_{0.4}Co_{0.2}Fe_{0.8}O_{3-\delta}$ membranes, Solid State Ionics, 180 (2009), pp. 241–245

46 W. Araki, J. Malzbender, Ferroelastic deformation of $La_{0.58}Sr_{0.4}Co_{0.2}Fe_{0.8}O_{3-\delta}$ under uniaxial compressive loading, J. Eur. Ceram. Soc., 33 (2013), pp. 805–812

47 J. J. Roa, A. Magrasó, M. Morales, P. Núñez, M. Segarra, Determination of hardness, Young's modulus and fracture toughness of lanthanum tungstates as novel proton conductors, Ceramics International, 37(5), 1593-1599 (2011).Figure Caption

Figure captions

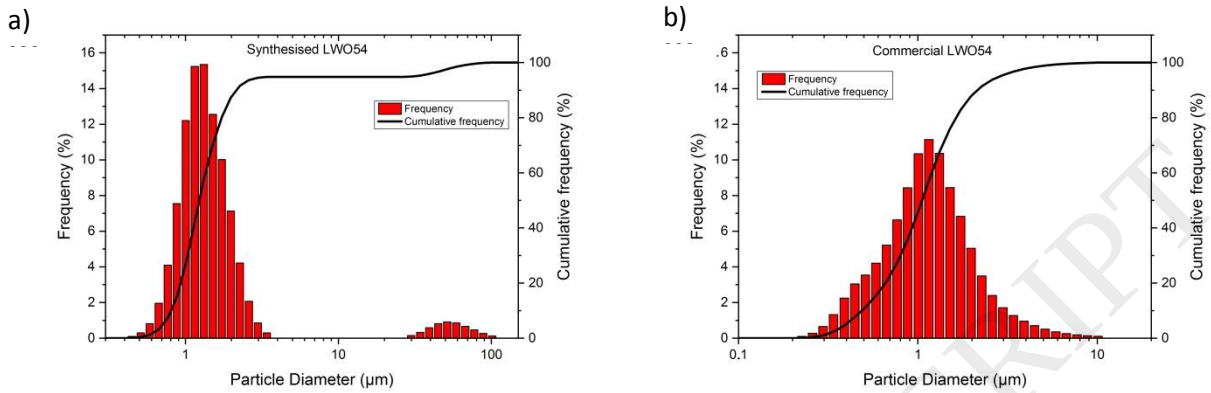

Figure 1: Particle size distribution of (a) the in-house synthesized LWO54-SSR-1 powder and (b) the commercial LWO54-SP-2 powder calcined at 1100 °C.

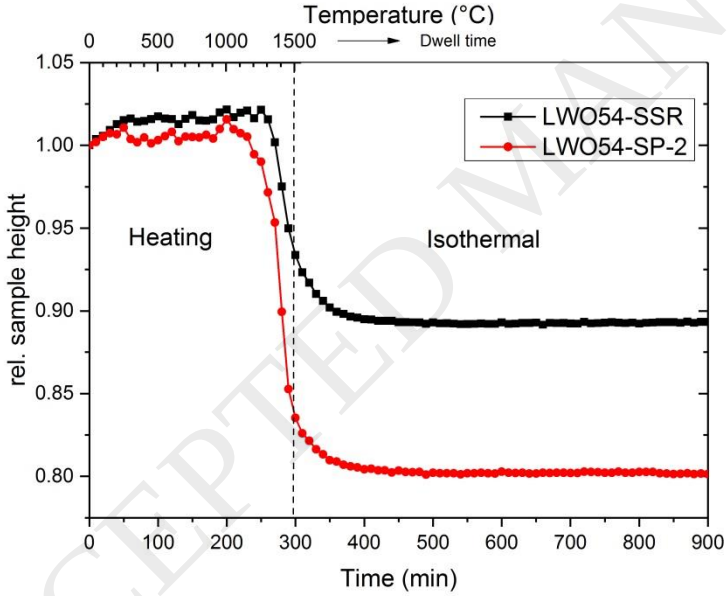

Figure 2: Shrinkage of pressed LWO54-SSR and LWO54-SP-2 powders sintered at 1500 °C for 10 h.

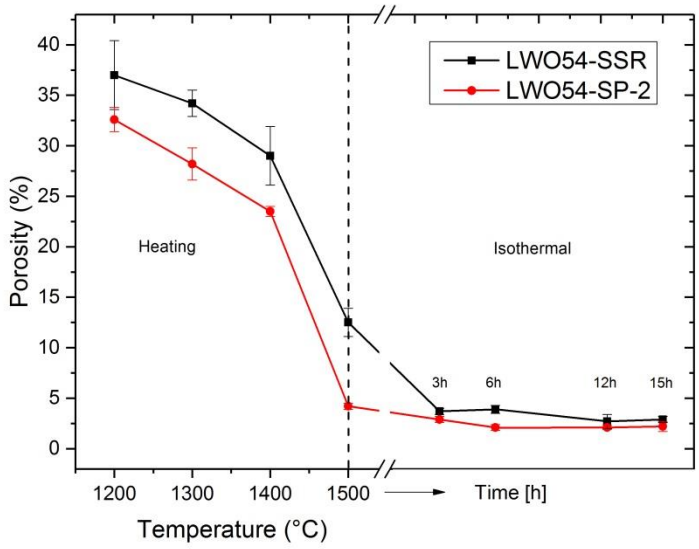

Figure 3: Porosity of LWO54-SSR and LWO54-SP-2 pellets during sintering at 1500 °C for 15 h obtained by SEM image analysis.

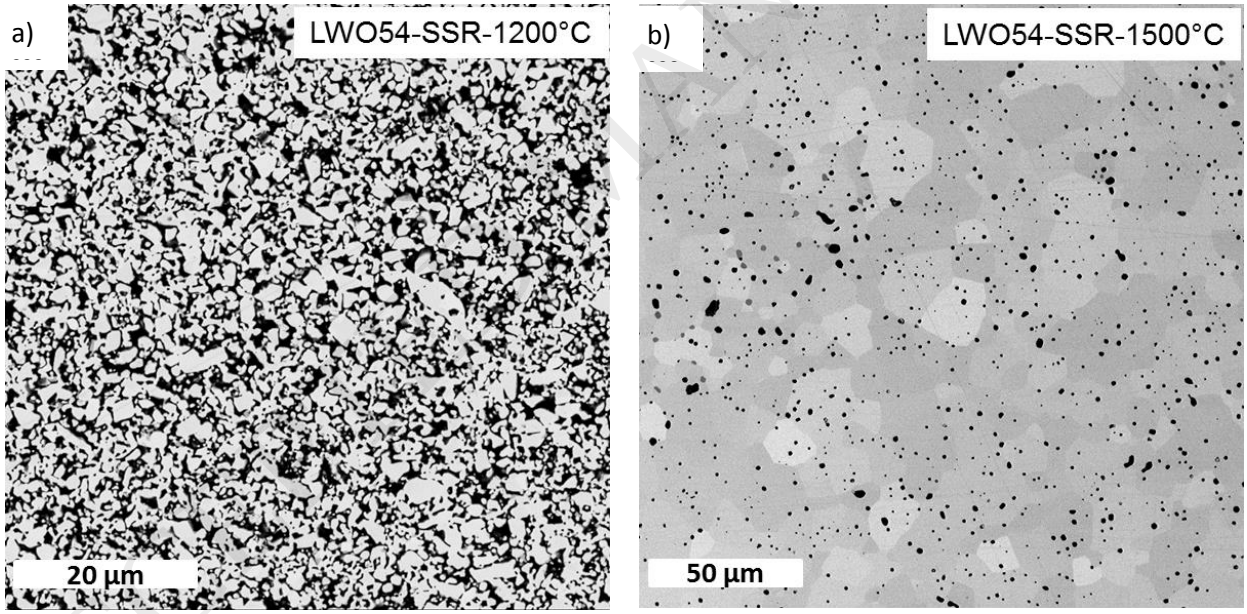

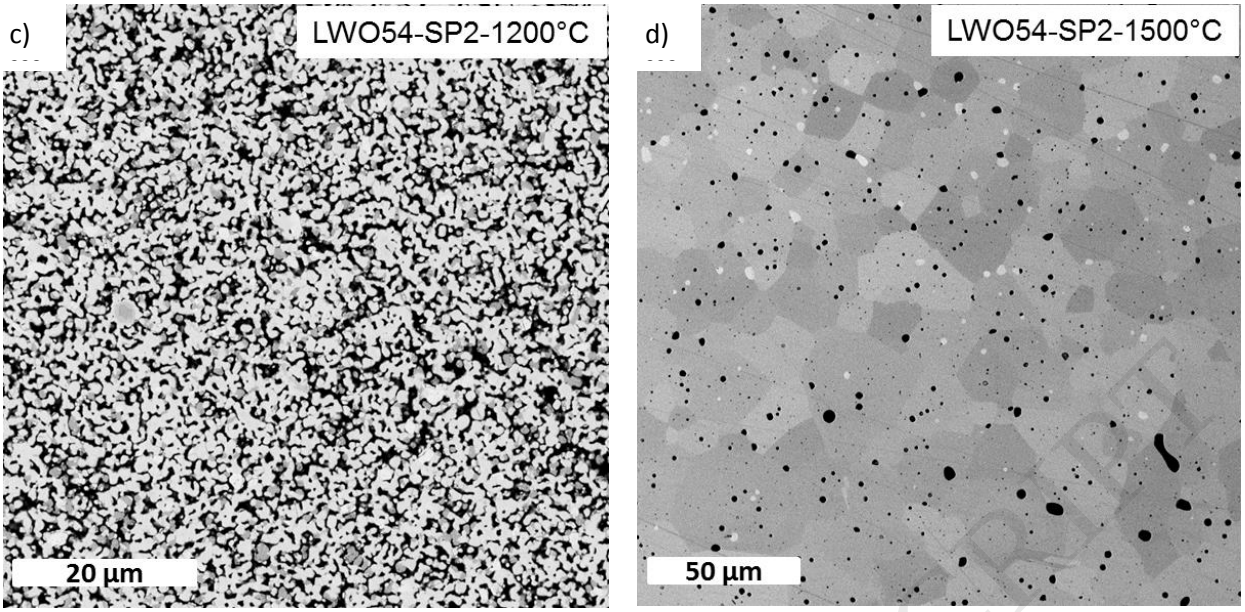

Figure 4: Microstructure of pressed specimens after sintering at 1200 °C and 1500 °C and 15 h holding time. (a) LWO54-SSR 1200 °C; (b) LWO54-SSR 1500 °C, 15 h; (c) LWO54-SP-2 1200 °C; (d) LWO-SP-2 1500 °C, 15 h.

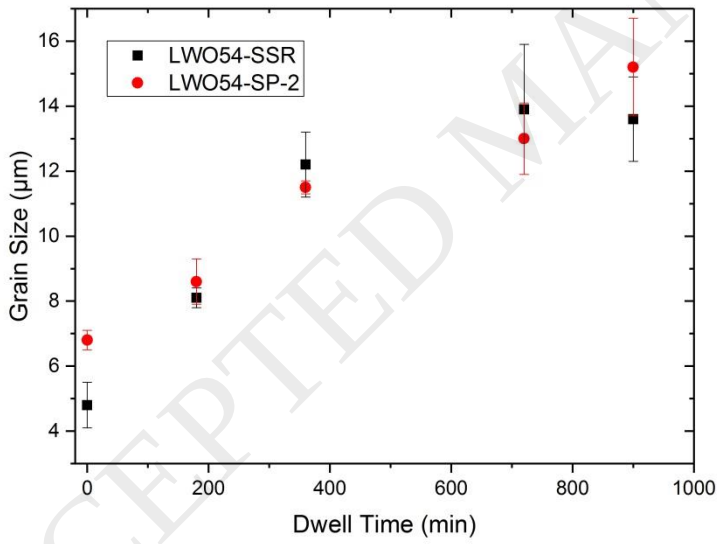

Figure 5: Grain size of sintered specimens made of LWO54-SSR and LWO54-SP-2 powders. Temperature is fixed at 1500°C and dwell time is varied between 0 and 12 h.

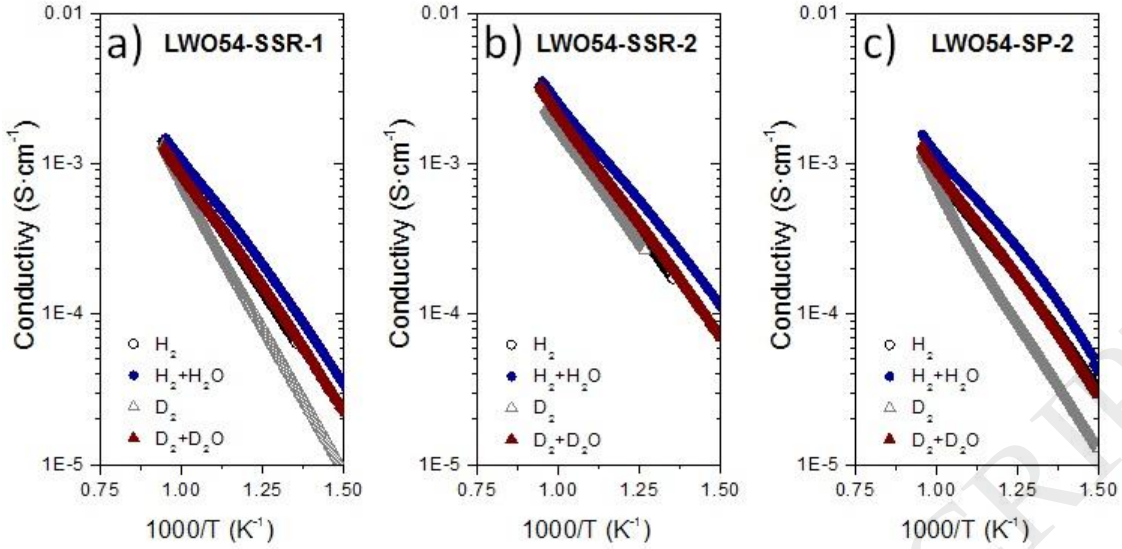

Figure 6: Total conductivity for LWO54-SSR-1, LWO54-SSR-2 and LWO54-SP-2 samples as a function of reciprocal temperature in H_2, D_2, H_2+H_2O and D_2+D_2O atmospheres (H_2 and D_2 diluted in 95% He).

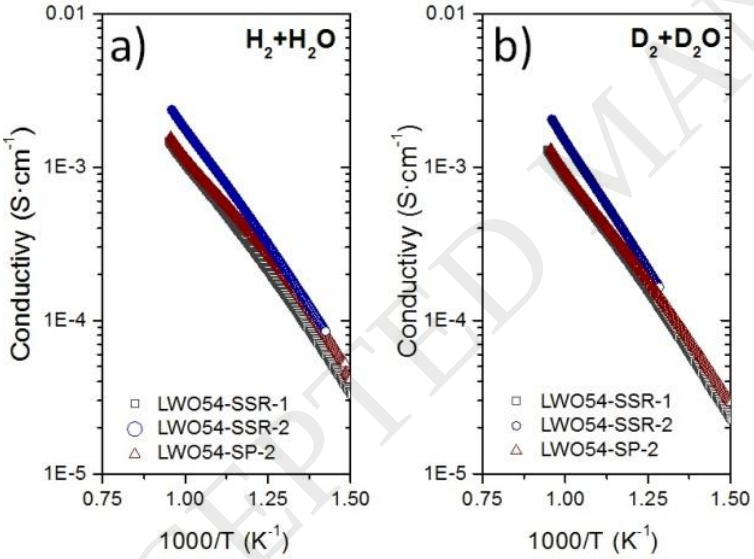

Figure 7: Total conductivity comparison of the three LWO54 samples with different grain size as a function of reciprocal temperature in (a) H_2+H_2O and (b) D_2+D_2O atmospheres (H_2 and D_2 diluted in 95% He).

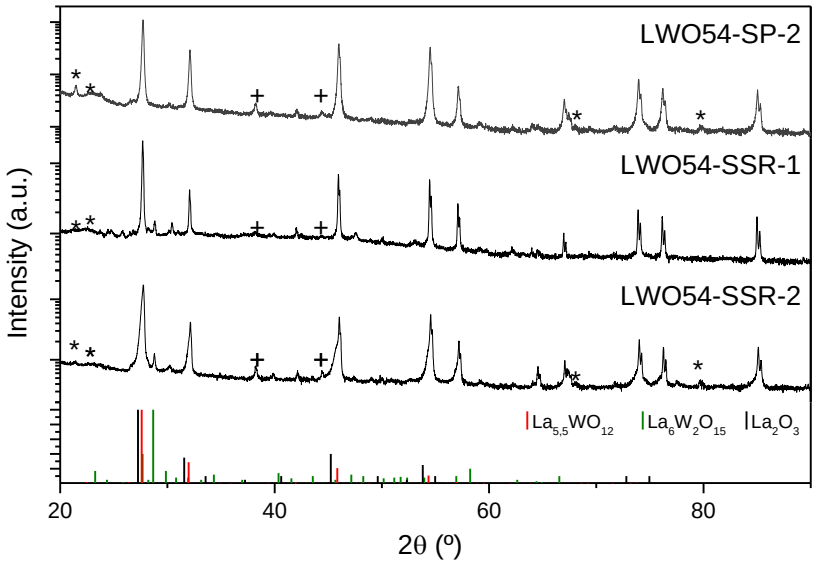

Figure 8: Room temperature XRD patterns of LWO54-SSR-1, LWO54-SSR-2 and LWO54-SP-2 as bars after the conductivity measurements (peaks corresponding to sample holder and silver used for the contacts are indicated as * and +, respectively).$La_{5.5}WO_{12}$, $La_6W_2O_{15}$ and La_2O_3 patterns were included for comparison.

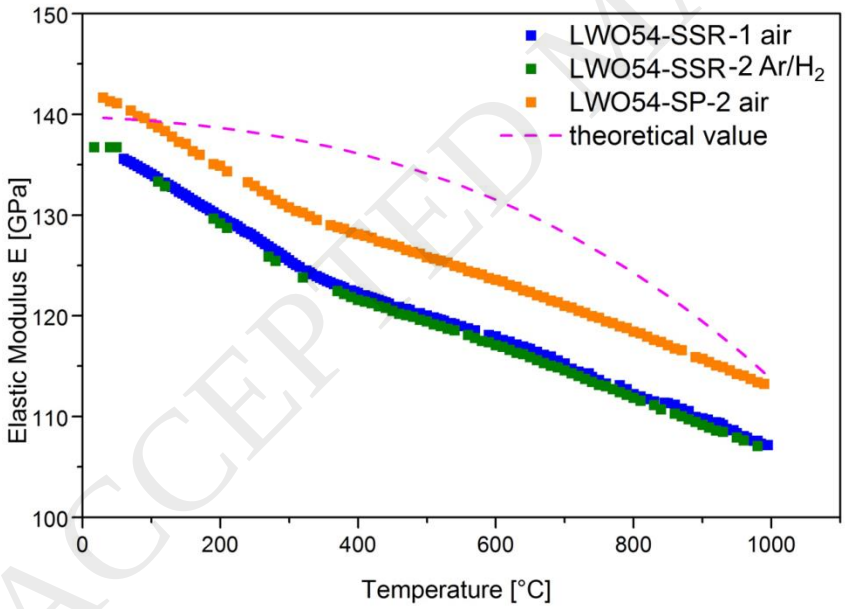

Figure 9: Elastic modulus of LWO54 in air (LWO54-SSR-1 and LWO-SP-2) and in Ar / 4% H_2 (LWO54-SSR-2) as a function of temperature measured by the impulse excitation technique. The dashed lines represent the model from Hillig [48].

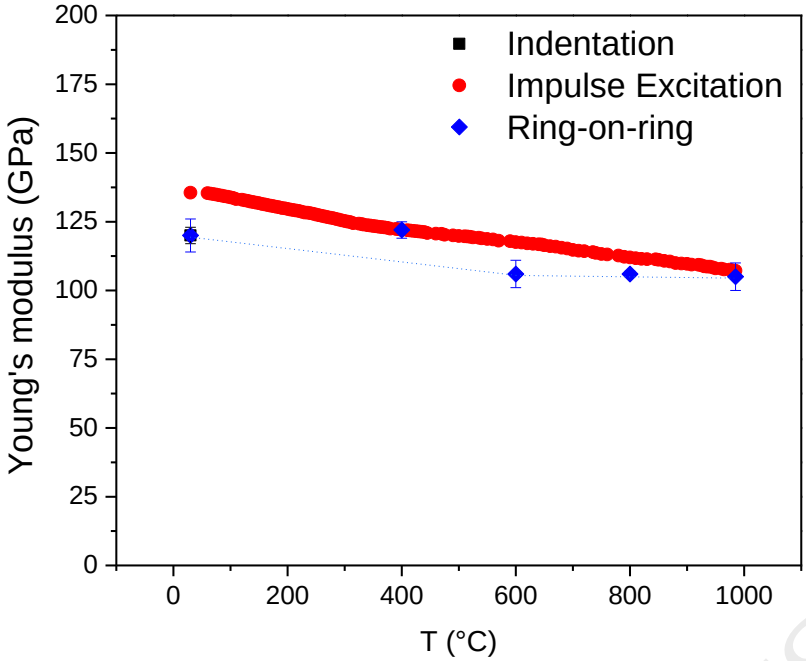

Figure 10: Evolution of Young's modulus with temperature for LWO54-SP-1 tested with impulse excitation and Ring-on-Ring method.

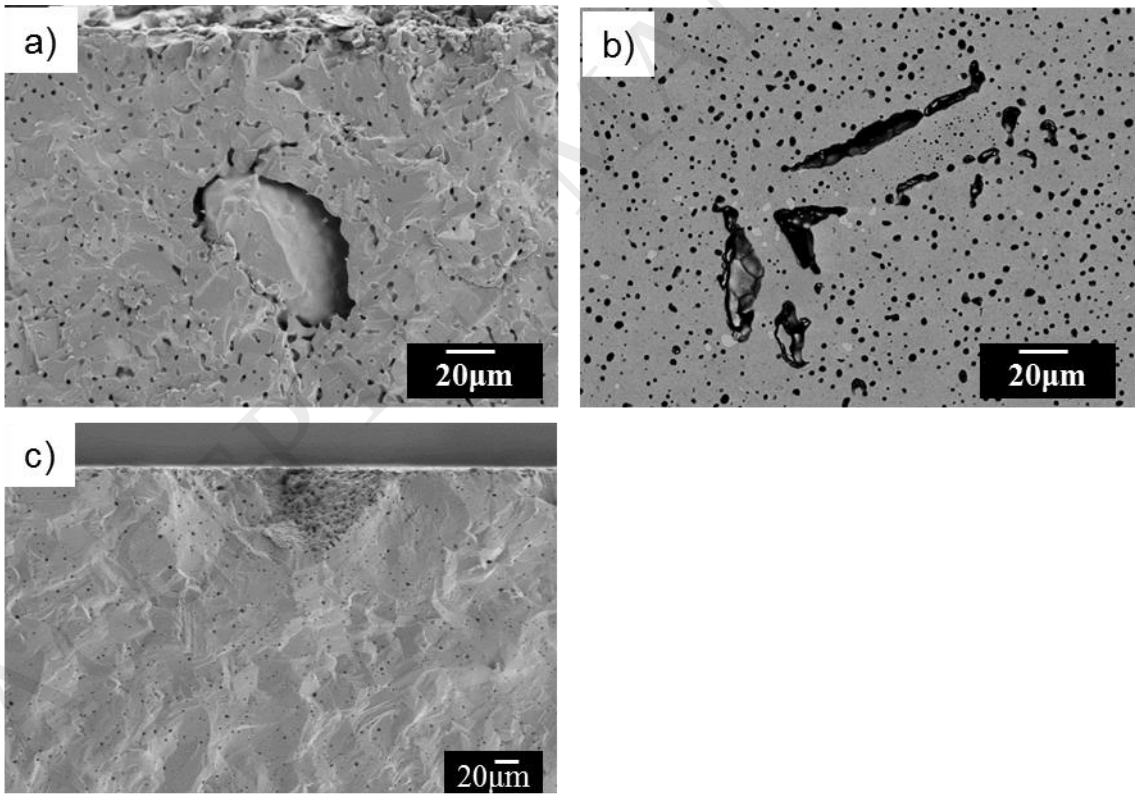

Figure 11: Microstructure of LWO54 -SP1 showing agglomerates as failure origin in a fracture surface σ_B =44MPa (a) and irregular pores and agglomerate in the polished cross section (b). LaWO54-SP-2 failure origin is a pore zone (c).

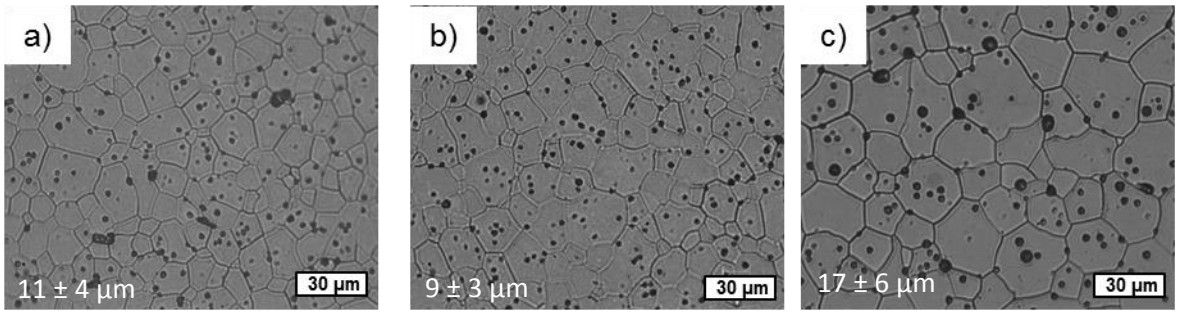

Figure 12 Microstructures of dense LWO54 specimens: (a) LWO-SSR-1, (b) LWO-SP-1 (c) LWO-SP-2.

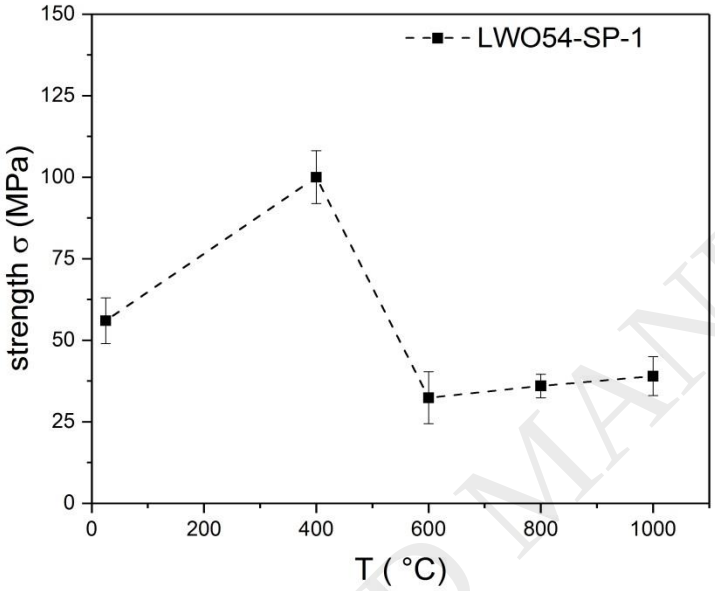

Figure 13: Dependence of strength on temperature (LWO54-SP-1 batch) at temperatures up to 1000 °C.

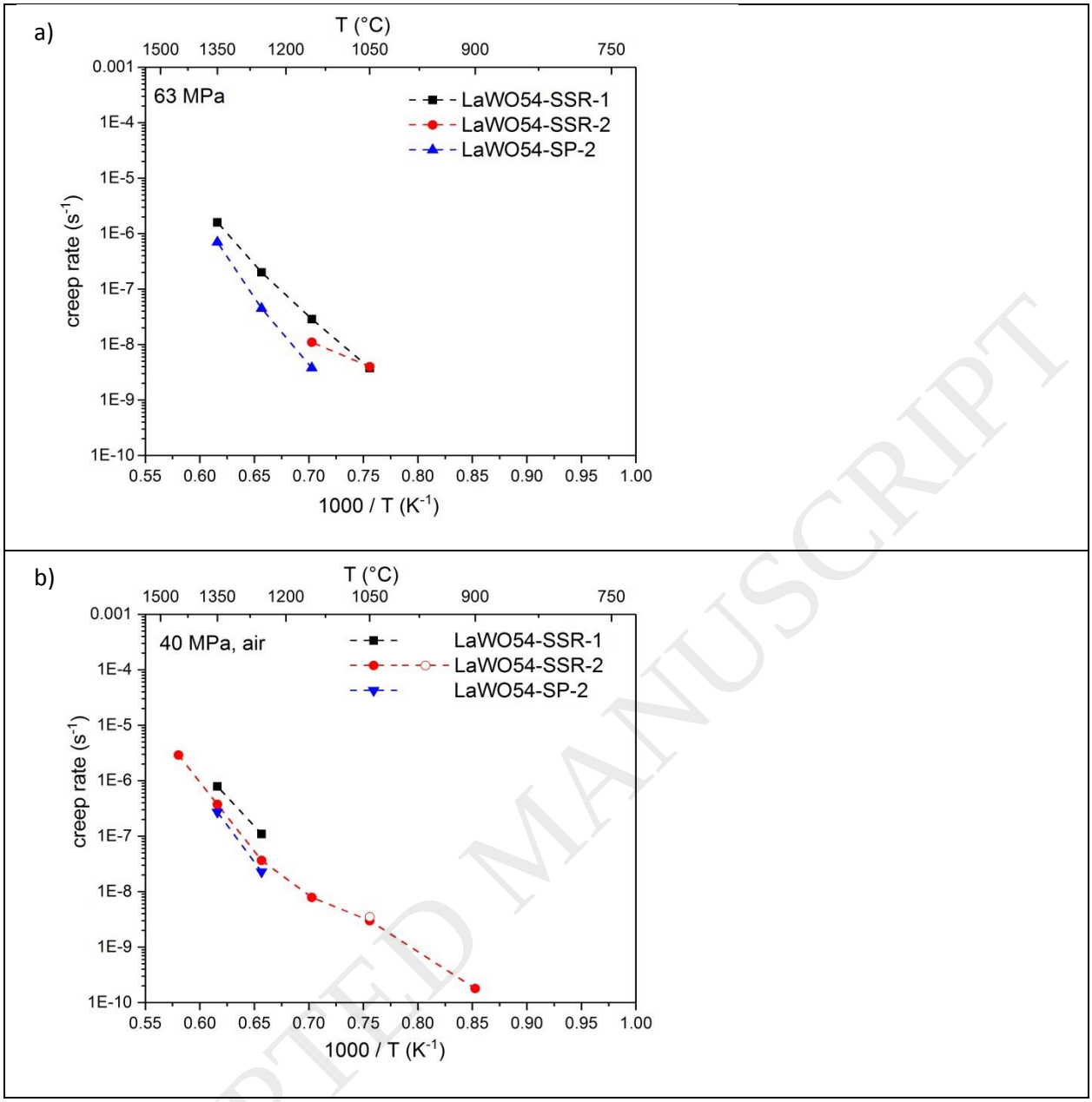

Figure 14: Arrhenius plots for LWO54 materials with applied stresses of 63 MPa (a) and 40 MPa (b) in air.

Table 1: List of samples tested for creep in compression.

Name of sample and geometry		**Test conditions**
LWO54-SSR-1	1 bar 3.3×4.2×12.0 mm^3	*T* = 700 °C - 1450 °C *T*-intervals = 100 °C or 150 °C σ = 20 - 63 MPa air
LWO54-SSR-2	1 bar 3.9×4×13.9 mm^3 1 cylinder 8.7 mm Ø 6.0 mm	
LWO54-SP-2	2 bars 3.6×3.8×14.8 mm^3	

Table 2: Powder characteristics of used LWO54 materials.

Powder	Specific Area (m^2/g)	D_{50} (µm)	Synthesis method
LWO54-SSR-1	1.9	1.2	Solid state reaction
LWO54-SP-2	3.3	1.1	Spray pyrolysis + calcination at 1100 °C

Table 3 Microstructural data of materials tested for electrical conductivity and creep.

Material	Sintering Temperature / Dwell Time (°C/ h)	Porosity (%)	Grain Size (µm)
LWO54-SSR-1	1500/3	12 ± 3	6 ± 3
LWO54-SSR-2	1500/12	3 ± 1	11 ± 4
LWO54-SP-2	1500/15	6 ± 1	17 ± 6

Table 4: Comparison of elastic moduli (GPa) of LWO54 samples determined with different methods.

Test Method	Elastic module (GPa)			Testing Conditions
	LWO54-SSR-1	LWO54-SP-1	LWO54-SP-2	
Ring-on-Ring (prepared surface)	120 ± 6	127 ± 6	130 ± 20	RT
Indentation	130 ± 2	120	94 ± 2	RT
Impulse Excitation	136	-	142	RT

Table 5: Summary of room temperature fracture stress tests for LWO54 materials.

	Batch name		
	LWO54-SSR-1	LWO54-SP-1	LWO54-SP-2
Number of specimens, *N*	13	9	9
Characteristic fracture strength σ_0 (MPa)	124	59	50
Mean fracture stress σ_B (MPa)	115 ± 20	56 ± 7	47 ± 7
Lower (0.95%) $t_{0.95}$ / upper (0.05%) $t_{0.05}$ Confidence bounds on σ_0	112 / 137	53.6 / 65.2	45.1 / 54.7
Biased Weibull Modulus w	6.2	8.7	8.0
Unbiased Weibull Modulus w_{ub}	5.5	7.2	6.7
Lower (0.95%) $q_{0.95}$ / upper (0.05%) $q_{0.05}$ Confidence bounds on w	3.4 / 7.2	3.8 / 9.9	3.5 / 9.2
Elastic Modulus (GPa)	120 ± 6	127 ± 6	130 ± 20
Fracture strain ε (%)	0.1	0.04	0.04

Table 6: Conditions for strength experiments on LWO54-SP-2 batch at 400°C.

Heating profile	Mean strength σ_B (MPa)	*E* (GPa)
Standard, heating to 400 °C	108 ± 10	122 ± 3
Heating to 1000 °C / cool to 400 °C	107	129
Heating to 400 °C / dwell 12 h	86	120

Table 7: Activation energies of LWO54 materials.

Stress (MPa)	LWO54-SSR-1		LWO54-SSR-2		LWO54-SP-2
	1050 – 1250°C	1250 – 1350°C	1050 – 1250°C	1250 - 1350°C	1250 - 1350°C
20	-	-	190 ± 40	380	-
40	-	405	210 ± 30	480	480
63	330 ± 10	420	-	--	565

Table 8: Stress exponents *n* for LWO54 materials.

Temperature (°C)	Stress exponent n	
	LWO54-SSR-1	LWO54-SSR-2
1050	-	0.60 ± 0.01
1150	-	0.80 ± 0.05
1250	1.20 ± 0.10	1.00
1350	1.20 ± 0.15	1.70
1450	-	1.20

Table 9: Inverse grain size exponent *p* for different stresses.

Temperature (°C)	Grain size exponent p	
	40 MPa	63 MPa
1150	-	1.9 ± 0.3
1250	1.5 ± 0.2	1.4
1350	1.0 ± 0.1	0.8